Pergamon

Acta mater. Vol. 45, No. 10, pp. 3949–3961, 1997

1359-6454/97 $17.00 + 0.00

PII: S1359-6454(97)00116-X

396

MICROSCOPIC MODEL FOR DIRECTIONAL COARSENING OF PRECIPITATES IN ALLOYS UNDER EXTERNAL LOAD

C. A. LABERGE[1]†, P. FRATZL[2] and J. L. LEBOWITZ[1]

[1]Department of Physics and Mathematics, Rutgers University, Piscataway, NJ 08855-0849, U.S.A. and [2]Institut für Materialphysik, Universität Wien, Boltzmanngasse 5, A-1090 Wien, Austria

(Received 26 August 1996; accepted 20 March 1997)

Abstract—We carried out computer simulations of a binary alloy decomposition in two dimensions under external stress using a Metropolis exchange dynamics with an effective long-range, anisotropic, "spin" Hamiltonian. This was obtained by minimizing the energy of elastic interactions between A and B atoms of unequal size, over the displacement of atoms from the equilibrium lattice sites. The evolution of configurations and the elastic strains associated with them were studied for various initial states. Directional coarsening was clearly visible in the precipitate morphology and was measured quantitatively both in the structure function and in the amount of interface pointing in the x or y direction. These were found to saturate at a fixed ratio, independent of the initial configuration: be it disordered or consisting of perfect stripes. This is due to an apparently inherent "waviness" of the precipitate interfaces. A suitably defined mean domain size increases with time in a manner consistent with a t^{α} behavior, with α between $\frac{1}{4}$ and $\frac{1}{3}$. © *1997 Acta Metallurgica Inc.*

1. INTRODUCTION

Directional coarsening or *rafting* is a well-known phenomenon, observed when certain alloys containing misfitting precipitates, like nickel-based superalloys, are subjected to uniaxial external load. Depending on conditions, a morphology consisting of either plate-like structures perpendicular to, or rod-like structures parallel to, the stress direction, develops. The phenomenon was discussed by Tien and Copley [1] and in many later studies [2–9]. The type of morphology depends on the signs of the misfit, on the load and on the difference between the elastic constants in matrix and precipitates. The systematics of this dependence (summarized in Table 1) have been established in a number of theoretical studies [11–13] and only a few exceptions to this rule have been reported in the literature [2]. To explain these exceptions, inelastic effects due to the movement of dislocations were considered in [2, 7–9]. Generally speaking it is unclear whether directional coarsening is due to elastic interactions or to the effects of dislocations, since large amounts of dislocations always appear during rafting even with moderate external stresses [10].

Since directional coarsening may considerably change the mechanical behavior of an alloy, it is important to understand the origins of the process as well as its kinetics. One of the approaches is to construct and study theoretical models for dislocation-induced rafting [2, 7–9], another is to consider elastic effects alone and determine how far experimental observations can be reproduced under such conditions. Previous theoretical modeling along those lines has been based mostly on considerations of the stability of precipitate shapes and arrangements [11–13], or on the use of a Ginzburg–Landau energy functional [14]. In [15] an approach combining finite-element analysis with a Monte-Carlo method was used.

In the present paper, we investigate a conceptually simple microscopic model which considers misfitting precipitates in an elastically anisotropic matrix, with only a small difference between the elastic constants inside and outside the precipitates. We consider only linear elasticity and completely leave out vacancies and dislocations. This not only simplifies the problem but will also, we hope, give a better understanding of the process of directional coarsening by separating the effects due to elasticity alone from those requiring the motion of dislocations. While the model is applicable in any dimension, we restricted ourselves here, for simplicity and availability of computational resources, to two dimensional systems. It is then a straightforward modification of one previously developed by Fratzl and Penrose [16, 17] describing phase separation in anisotropic alloy systems with elastic misfit. In a recent short communication [19] we have shown that our model predicts the development of wavy stripes, much like those seen in experiments [10], and that it can be used to study the kinetics of symmetry breaking due to the external stress. Here we give a detailed derivation of the model and discuss

†Present address: Department of Physics, Virginia Polytechnic Institute, Blacksburg, VA 24061-0435, U.S.A.

the kinetics for alloys with high (50%) and with low (20%) volume fraction of precipitates.

2. THE MODEL

We start by treating the problem in terms of continuum elasticity. Suppose that an alloy contains two types of atoms, A and B, of different size ($R_A > R_B$). During decomposition, the regions containing predominantly A-atoms will want to have a larger lattice spacing than those containing predominantly B-atoms. If the strains associated with these differences are assumed to be purely dilatational, that is to have no shear components, the strain tensor at a position $\mathbf{r}$ in the sample is diagonal and can be written as $\epsilon^T(\mathbf{r})\,\delta ij$, where δ_{ij} is the Kronecker symbol. The value of $\epsilon^T(\mathbf{r})$ is directly related to the local composition at $\mathbf{r}$; it is positive (negative) in regions containing an excess of A-atoms (B-atoms) compared to the average. The stress tensor $\sigma_{ij}^T = \Lambda_{ijkl}\epsilon^T\delta_{kl}$ (where Λ_{ijkl} is the tensor of elastic constants and we use the convention of summation over repeated indices) can be thought of as the stress required to remove these lattice spacing inhomogeneities. We will study here the influence of an additional *external* homogeneous stress σ_{ij}^0 superposed on these internal stresses.

Denoting by $\epsilon_{ij}(\mathbf{r})$ the total strain at a given position $\mathbf{r}$ in the material, the elastic energy can be written [13] as $W = \int w\, d^3\mathbf{r}$, where

$$w = \tfrac{1}{2}\Lambda_{ijkl}(\epsilon_{ij} - \epsilon^T\delta_{ij})(\epsilon_{kl} - \epsilon^T\delta_{kl}) - \sigma_{ij}^0\epsilon_{ij}. \qquad (1)$$

The first term in (1) represents the relaxation energy of the system and the second term is the work done by the external stress.

We now assume that the elastic constants have a weak dependence on the local composition or, equivalently, on $\epsilon^T(\mathbf{r})$. To a first approximation, we write

$$\Lambda_{ijkl}(\epsilon^T) = (1 + \alpha\epsilon^T(\mathbf{r}))\Lambda_{ijkl}^0, \qquad (2)$$

where Λ_{ijkl}^0 is the usual, position independent, elastic tensor of the homogeneous material, and α a small constant; $\alpha > 0$ means that the elastic constants are larger in the regions with larger equilibrium lattice spacing (that is, $\epsilon^T(\mathbf{r}) > 0$). Since the strains ϵ_{ij}^0, related to the applied stress by $\sigma_{ij}^0 = \Lambda_{ijkl}^0\,\epsilon_{ij}^0$, are uniform throughout the system we can rewrite the elastic energy (1) in terms of new strains $v_{ij} = \epsilon_{ij} - \epsilon_{ij}^0$ and get $W = \text{constant} + \int w'\, d^3\mathbf{r}$, where

$$w' = \tfrac{1}{2}\Lambda_{ijkl}^0 v_{ij}v_{kl} - \epsilon^T\Lambda_{ijkl}^0 v_{ij} \times \{\delta_{kl} - \alpha(\epsilon_{kl}^0 + \tfrac{1}{2}v_{kl} - \epsilon^T\delta_{kl})\} + \tfrac{1}{2}(\epsilon^T)^2\Lambda_{ijkl}^0\delta_{ij}\{\delta_{kl} - 2\alpha(\epsilon_{kl}^0 - \epsilon^T\delta_{kl})\}. \qquad (3)$$

When $\alpha = 0$ then (3) is similar to (1) with $\epsilon_{ij} \to v_{ij}$ but *without* external stress (which has been absorbed into the constant term). One thus sees that in order to observe non-trivial effects due to the presence of an external stress we need $\alpha \neq 0$ in (2) above. We shall be interested in the case where $\alpha\epsilon^T(\mathbf{r}) \ll 1$, such that the true elastic constants differ only slightly from the ones where $\alpha = 0$. Furthermore we assume that the *external* stresses are large enough for v_{ij} and $\epsilon^T\delta_{ij}$ to be neglected in comparison with ϵ_{ij}^0 in the correction term proportional to α. The product $\alpha\epsilon_{ij}^0$ is taken to be small but not negligible. Making this approximation yields an expression for the elastic energy density:

$$w' \approx \tfrac{1}{2}\Lambda_{ijkl}^0\{v_{ij}v_{kl} - 2\epsilon^T v_{ij}(\delta_{kl} - \alpha\epsilon_{kl}^0) + (\epsilon^T)^2\delta_{ij}(\delta_{kl} - 2\alpha\epsilon_{kl}^0)\} \qquad (4)$$

or, equivalently,

$$w' \approx \tfrac{1}{2}\Lambda_{ijkl}^0[v_{ij} - (\delta_{ij} - 2\alpha\epsilon_{ij}^0\epsilon^T)][v_{kl} - \epsilon^T\delta_{kl}], \qquad (5)$$

which is a quadratic function of the strain v_{ij}. The minimization with respect to the v_{ij} can now be done easily and the effective potential calculated explicitly, at least in Fourier space.

2.1. *Microscopic model*

In order to obtain a microscopic Hamiltonian corresponding to the continuum theory above, we start with the basic model described in [16, 17], referred to as I and II, respectively. (Another atomistic approach, not including external stresses, is also described in [18].) It consists of A and B-atoms on a planar square lattice $\mathcal{L}$ with periodic boundary conditions. A spin variable $\gamma(\mathbf{p})$ is assigned at each site $p \in \mathcal{L}$, with $\gamma(\mathbf{p}) = 1$ if there is an A-atom at site $\mathbf{p}$ and $\gamma(\mathbf{p}) = -1$ if there is a B-atom there. The deviation of the position of an atom from its lattice site $\mathbf{p}$ is denoted by the vector $\mathbf{u}(\mathbf{p})$. The atoms are connected by elastic springs in a way shown in Fig. 1: springs with longitudinal (L_+) and transverse (T_+) stiffness between nearest neighbors and springs with longitudinal stiffness ($L_\times$) between next nearest neighbors.

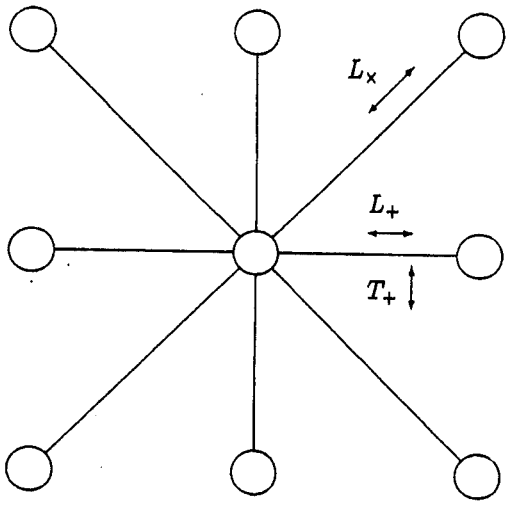

Fig. 1. Couplings L_+, $L_\times$ and T_+ between neighboring atoms.

The distortion introduced by the different sizes of the atoms is, as in I, related to

$$\eta(\mathbf{p}) = \tfrac{1}{2}(R_A - R_B)[\gamma(\mathbf{p}) - (2\bar{c} - 1)], \qquad (6)$$

where R_A and R_B are the radii of A and B atoms (or ions), respectively, and $\bar{c}$ is the average concentration of A-atoms in the alloy. The constant term in (6) is chosen to make the sum of $\eta(\mathbf{p})$ over the whole system vanish. Furthermore the linear dependence (2) of the elastic constants on the transformation strain in the continuum model becomes here, in the atomic model, a linear dependence of the coupling constants on η. Thus we replace the position independent spring constants used in I by:

$$L_+ \to L_+^0[1 + \alpha(\eta(\mathbf{p}) + \eta(\mathbf{p}'))];$$
$$L_\times \to L_\times^0[1 + \alpha(\eta(\mathbf{p}) + \eta(\mathbf{p}'))/\sqrt{2}], \qquad (7)$$

where $\mathbf{p}$ and $\mathbf{p}'$ are the lattice sites connected by the springs, and we assumed for simplicity that T_+ does not depend on η. From now on we will drop the superscript 0 on the spring couplings. In analogy with the continuum case discussed earlier we keep only those terms in α which are of the form αc_{ij}^0. We also introduce the variable $v_i(\mathbf{p})$ describing the displacement $u_i(\mathbf{p})$ relative to the homogeneous strain:

$$v_1(\mathbf{p}) = u_1(\mathbf{p}) - \frac{(\mathbf{p}\cdot\mathbf{e}_1)}{a}\epsilon_{11}^0 - \frac{1}{2}\frac{(\mathbf{p}\cdot\mathbf{e}_2)}{a}\epsilon_{12}^0,$$

$$v_2(\mathbf{p}) = u_2(\mathbf{p}) - \frac{1}{2}\frac{(\mathbf{p}\cdot\mathbf{e}_1)}{a}\epsilon_{12}^0 - \frac{(\mathbf{p}\cdot\mathbf{e}_2)}{a}\epsilon_{22}^0,$$

where $\mathbf{e}_i$ denotes a unit vector in the i direction ($i = 1, 2$), $u_i(\mathbf{p}) = \mathbf{u}(\mathbf{p})\cdot\mathbf{e}_i$ is the i-component of the displacement vector $\mathbf{u}(\mathbf{p})$, and a is the lattice spacing. With these definitions, the sum of $v_i(\mathbf{p})$ over the lattice vanishes. The microscopic elastic Hamiltonian H_{el} corresponding to (5) can thus be written as

$$\begin{aligned}
H_{el} = {} & \frac{1}{2}L_+ \sum_{\mathbf{p}} \sum_{i=1,2} \{(v_i(\mathbf{p} + a\mathbf{e}_i) - v_i(\mathbf{p}) \\
& -(1 - 2\alpha c_{ii}^0)[\eta(\mathbf{p} + a\mathbf{e}_i) + \eta(\mathbf{p})]\} \\
& \times \{(v_i(\mathbf{p} + a\mathbf{e}_i) - v_i(\mathbf{p}) - [\eta(\mathbf{p} + a\mathbf{e}_i) + \eta(\mathbf{p})]\} \\
& + \frac{1}{2}T_+ \sum_{\mathbf{p}} \{[(v_2(\mathbf{p} + a\mathbf{e}_1) - v_2(\mathbf{p})]^2 \\
& + [(v_1(\mathbf{p} + a\mathbf{e}_2) - v_1(\mathbf{p})]^2\} \\
& + \frac{1}{2}L_\times \sum_{\mathbf{p}} \sum_{\mu=\{+1,-1\}} \{v_1(\mathbf{p} + a\mathbf{e}^{(\mu)}) \\
& + \mu v_2(\mathbf{p} + a\mathbf{e}^{(\mu)}) - v_1(\mathbf{p}) - \mu v_2(\mathbf{p})]/\sqrt{2} \\
& -[1 - \alpha(\epsilon_{11}^0 + \epsilon_{22}^0 + \mu\epsilon_{12}^0)][\eta(\mathbf{p} + a\mathbf{e}^{(\mu)}) + \eta(\mathbf{p})]\} \\
& \times \{[v_1(\mathbf{p} + a\mathbf{e}^{(\mu)}) + \mu v_2(\mathbf{p} + a\mathbf{e}^{(\mu)}) - v_1(\mathbf{p}) \\
& -\mu v_2(\mathbf{p})]/\sqrt{2} - [\eta(\mathbf{p} + a\mathbf{e}^{(\mu)}) + \eta(\mathbf{p})]\} \qquad (8)
\end{aligned}$$

where $\mathbf{e}^{(\mu)} = \mathbf{e}_1 + \mu\mathbf{e}_2$, $\mu = \pm 1$, in the $L_\times$ term.

Table 1. Rafting morphology developing in an alloy with negative elastic anisotropy ($\Delta < 0$) under uniaxial load along x. $\perp$ and $\parallel$ mean that the stripes which are developing are oriented, respectively, perpendicular or parallel to the direction of the load

Lattice spacing in precipitates	Elastic constants in precipitates	External load along x	ζ	Morphology
Larger	Larger	Tensile	>0	$\parallel$
Larger	Larger	Compressive	<0	$\perp$
Larger	Smaller	Tensile	<0	$\perp$
Larger	Smaller	Compressive	>0	$\parallel$
Smaller	Larger	Tensile	<0	$\perp$
Smaller	Larger	Compressive	>0	$\parallel$
Smaller	Smaller	Tensile	>0	$\parallel$
Smaller	Smaller	Compressive	<0	$\perp$

The elastic Hamiltonian (8) has a quadratic form similar to (4)

$$H_{el}(\Gamma, \mathbf{V}) = \tfrac{1}{2}\mathbf{V}\cdot\mathscr{D}\cdot\mathbf{V} + \mathbf{G}\cdot\mathbf{V}\Gamma + \Omega\Gamma^2, \qquad (9)$$

where Ω is a scalar function, $\mathbf{G}$ and $\mathbf{V}$ should be thought of as vectors with $2N$ components, and $\mathscr{D}$ as a $2N \times 2N$ matrix, where N is the total number of sites in the lattice $\mathscr{L}$. The quantity $\mathbf{V}$ is specified by the displacements $\{v(\mathbf{p})\}$, and Γ by the configuration $\{\gamma(\mathbf{p})\}$.

Since the diffusion time and the vibrational relaxation time of the atoms are such that $\tau_{vib} \ll \tau_{diff}$, it is reasonable to assume that $\mathbf{V}$ reaches its equilibrium state for a given configuration Γ (in the sense that the total elastic energy has reached its minimum) by the time an atom diffuses to another site. This greatly simplifies the problem when the Hamiltonian has the form (9) above, since the minimization of H with respect to $\mathbf{V}$ yields a *linear* set of equations between the displacement $\mathbf{V}$ and the configuration Γ which can be easily solved in Fourier space [21, 22]. Note that since (9) is quadratic in $\mathbf{V}$, the minimization also corresponds to replacing the displacements by their average values in an equilibrium canonical ensemble with a specified configuration Γ. However in this case H_{el} would also depend on the temperature, which we ignore here since we are primarily interested in the kinetics at a fixed temperature.

In addition to the elastic interaction we introduce a short range "chemical interaction" between the atoms. For simplicity we restrict this here to nearest neighbors. It then has the form of a ferromagnetic Ising Hamiltonian form

$$H_{chem} = -J \sum_{\mathbf{p}\in\mathscr{L}} \sum_{i=1,2} \gamma(\mathbf{p})\gamma(\mathbf{p} + a\mathbf{e}_i), \quad J > 0. \qquad (10)$$

We expect that below a certain critical temperature T_C, which will be shifted from the Onsager value of $T_0 = 2.27J/k_B$ because of the elastic interaction, there will be a segregation between regions mostly occupied by A-atoms and regions mostly occupied by B-atoms.

After the minimization over the atomic displacements, the total Hamiltonian can be written as

$$H_{\text{tot}} = \frac{1}{2N} \sum_{\mathbf{k} \in BZ} \tilde{\Psi}(\mathbf{k}) |\tilde{\gamma}(\mathbf{k})|^2$$

$$= \frac{1}{2N} \sum_{\mathbf{p},\mathbf{p}' \in \mathscr{L}} \Psi(\mathbf{p} - \mathbf{p}') \gamma(\mathbf{p}) \gamma(\mathbf{p}'), \qquad (11)$$

where $\tilde{\gamma}(\mathbf{k})$ and $\tilde{\Psi}(\mathbf{k})$ are the Fourier transforms of $\gamma(\mathbf{p})$ and the effective pair potential $\Psi(\mathbf{p} - \mathbf{p}')$, respectively,

$$\tilde{\gamma}(\mathbf{k}) = \sum_{\mathbf{p}} \gamma(\mathbf{p}) e^{i\mathbf{k}\cdot\mathbf{p}}; \quad \tilde{\Psi}(\mathbf{k}) = \sum_{\mathbf{p}} \Psi(\mathbf{p}) e^{i\mathbf{k}\cdot\mathbf{p}}$$

and the sum over $\mathbf{k}$ in (11) is taken over the first Brillouin zone of the lattice $\mathscr{L}$.

The effective potential $\Psi(\mathbf{p})$ contains a *long range anisotropic* elastic part $\Psi_{\text{el}}^{\text{eff}}(\mathbf{p})$ which has a form similar to a dipole–dipole interaction and decays like r^{-2} (r^{-3} in three dimensions) at large distances r. It also contains a short-range part $\Psi_{\text{sh}}(\mathbf{p})$ which receives contribution from the chemical interaction (10) as well as from the elastic interaction term of the form $\Omega\Gamma^2$ in (9). In Fourier space the potential $\tilde{\Psi}(\mathbf{k})$, which is the sum of $\tilde{\Psi}_{\text{sh}}(\mathbf{k}) + \tilde{\Psi}_{\text{el}}^{\text{eff}}(\mathbf{k})$, can be calculated explicitly:

$$\tilde{\Psi}_{\text{sh}}(\mathbf{k}) = -2J(\cos ak_1 + \cos ak_2) + \tfrac{1}{2}\lambda J \tilde{\Omega}, \quad (12)$$

$$\tilde{\Psi}_{\text{el}}^{\text{eff}}(\mathbf{k}) = -\frac{1}{2}\lambda J \frac{\tilde{\mathscr{D}}_{22}\tilde{G}_1^2 + \tilde{\mathscr{D}}_{11}\tilde{G}_2^2 - 2\tilde{\mathscr{D}}_{12}\tilde{G}_1\tilde{G}_2}{\tilde{\mathscr{D}}_{11}\tilde{\mathscr{D}}_{22} - \tilde{\mathscr{D}}_{12}^2}, \quad (13)$$

with $\lambda = (R_A - R_B)^2/J$,

$$\tilde{\Omega} = \sum_{i=1}^{2} \{(1 - 2\alpha\epsilon_{ii}^0)(1 + c_i)L_+ + [1 - \alpha(\epsilon_{11}^0 + \epsilon_{22}^0)](1 + c_1c_2)L_\times\}$$

and

$$\tilde{G}_i = s_i(1 - \alpha\epsilon_{ii}^0)L_+ - [c_{3-i}s_i(1 - \alpha(\epsilon_{11}^0 + \epsilon_{22}^0)/2) - c_i s_{3-i}\alpha\epsilon_{12}^0/2]\sqrt{2}L_\times$$

$$\tilde{\mathscr{D}}_{ij} = \delta_{ij}\{(1 - c_i)L_+ + (1 - c_{3-i})T_+ + (1 - c_1c_2)L_\times\} + (1 - \delta_{ij})s_1s_2L_\times.$$

Here $i \in \{1, 2\}$, $c_i = \cos ak_i$, and $s_i = \sin ak_i$, k_1 and k_2 being the components of the vector $\mathbf{k}$ along the x and y directions of the square lattice.

2.2. *Long wave length limit and continuum description*

As stated previously the short-range interaction will induce, below some critical temperature T_c, a phase segregation between A-rich and B-rich regions. To get an idea of the influence of the anisotropic and long-range character of the effective elastic potential on the segregation process we look at the $\mathbf{k} \to 0$ behavior of $\tilde{\Psi}_{\text{el}}(\mathbf{k})$. This corresponds to the Fourier transform of the effective elastic potential in the corresponding continuum model. We find, dropping the α^2 terms,

$$\lim_{|\mathbf{k}|\to 0} \tilde{\Psi}_{\text{el}}^{\text{eff}}(\mathbf{k}) = Y(\hat{\mathbf{k}}) + \text{constant}$$

where

$$Y(\hat{\mathbf{k}}) = -Y_0 \frac{1 + 2\Delta(\hat{k}_1\hat{k}_2)^2 - \chi_{ij}\hat{k}_i\hat{k}_j}{1 + \xi\Delta(\hat{k}_1\hat{k}_2)^2}, \qquad (14)$$

and $\hat{\mathbf{k}} = \mathbf{k}/|\mathbf{k}|$, $\hat{k}_1 = k_1/|\mathbf{k}| = \cos\theta$, $\hat{k}_2 = \sin\theta$. In our model the parameter Y_0, which specifies the strength of the elastic energy relative to the chemical energy parameter J, is given by

$$Y_0 = \lambda J[1 - \alpha(\epsilon_{11}^0 + \epsilon_{22}^0)] \frac{(L_+ + \sqrt{2}L_\times)^2}{L_+ + L_\times}. \qquad (15)$$

The continuum elastic properties of the material enter

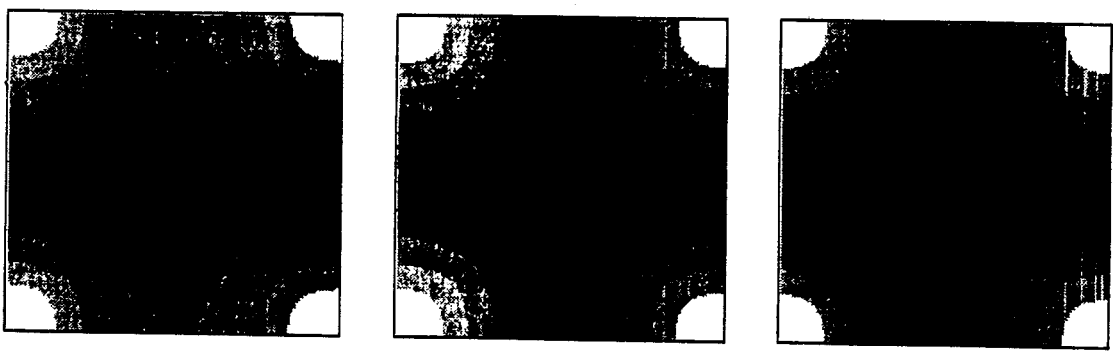

Fig. 2. Potential $\tilde{\Psi}(\mathbf{k})$ represented in the first Brillouin zone of the square lattice using a pseudo-grey scale. The lowest values of the potential are dark, while the highest are white. The origin of $\mathbf{k}$ is in the center of the picture. The left picture shows the case $\zeta = -0.1$ (compressive stress along the horizontal), the center picture shows $\zeta = 0$ (no external stress) and the right $\zeta = 0.1$ (tensile stress along the horizontal).
The elastic constants were assumed to be larger in the phase with larger lattice spacing ($\alpha > 0$).

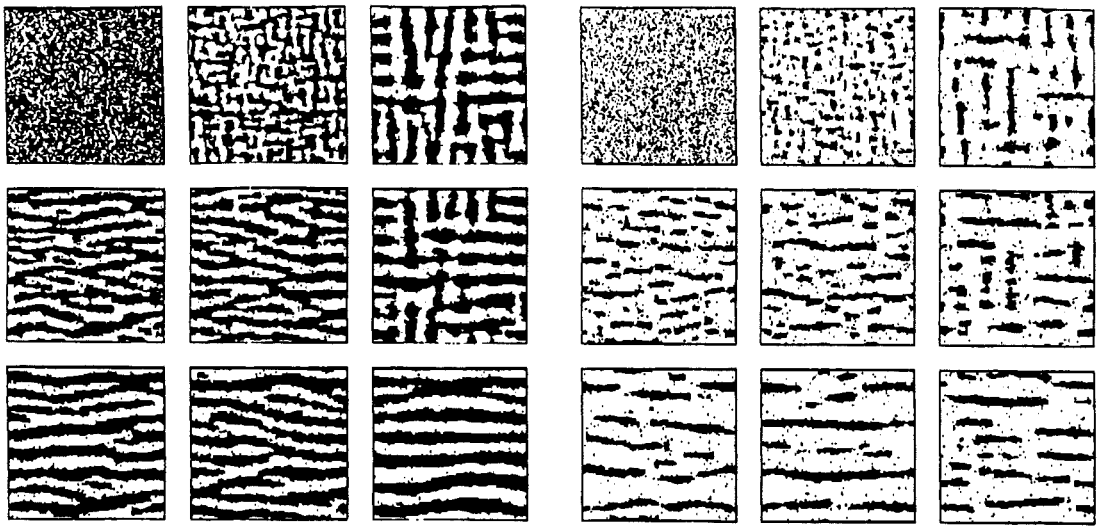

Fig. 3. Snapshot configurations for alloys with composition at $c = 0.5$ (left) and $c = 0.2$ (right) at the temperature $T = 1.8J/k_B$ on a 128×128 lattice. The top row shows an evolution of the alloys without external stress ($\zeta = 0$) starting from random distribution of the atoms after 0, 10^3 and 10^4 Monte Carlo steps. The second row shows the change of the top row configurations after annealing under external stress ($\zeta = 0.1$) for 10^3 MCS. The bottom row shows the same after 10^4 MCS.

through the parameters Δ and ξ

$$\Delta = \frac{L_+ - 2L_\times - T_+}{T_+ + L_\times} = \frac{C_{11}^0 - C_{12}^0 - 2C_{44}^0}{C_{44}^0};$$

$$\xi = \frac{L_+ + 2L_\times - T_+}{L_+ + L_\times} = \frac{C_{11}^0 + C_{12}^0}{C_{11}^0}, \qquad (16)$$

where we have used the relationship between our spring constants $\{L_+, T_+, L_\times\}$ and the elastic constants of the material, for a simple cubic lattice,

$$C_{11}^0 = L_\times + L_+;$$

$$C_{12}^0 = L_\times - T_+; \quad C_{44}^0 = L_\times + T_+. \qquad (17)$$

The external stress shows up in the traceless tensor χ_{ij}

$$\chi_{11} = -\chi_{22} = \alpha(\epsilon_{11}^0 - \epsilon_{22}^0)\frac{L_+}{L_+ + \sqrt{2}L_\times};$$

$$\chi_{12} = \alpha\epsilon_{12}^0 \frac{L_+ + T_+}{L_\times + T_+}\frac{\sqrt{2}L_\times}{L_+ + \sqrt{2}L_\times}, \qquad (18)$$

with χ_{11} proportional to the uniaxial load (or stretch) on the system, and χ_{12} proportional to the external shear.

The important elastic effects on the coarsening all come from the long range elastic potential that decays like r^{-2} (r^{-3} in three dimensions). When $Y_0 = 0$ in (14), as happens when $R_A = R_B$, we expect the model to be in the same universality class as model B of [23]. In general, we expect that the kinetics will be described on the macroscopic scale by a Cahn–Hilliard type equation [24, 25], for the local concentration

$$\frac{\partial c(\mathbf{r}, t)}{\partial t} = \nabla \cdot \left\{ \sigma(c) \nabla \frac{\delta}{\delta c(\mathbf{r}, t)} \int d\mathbf{r} \left[f(c) \right.\right.$$

$$\left.\left. + \frac{1}{2}\lambda |\nabla c|^2 + \int d\mathbf{r}' Y(\mathbf{r} - \mathbf{r}') c(\mathbf{r}', t) c(\mathbf{r}, t) \right] \right\}. \qquad (19)$$

Here $\sigma(c)$ is the mobility tensor that can be concentration dependent, and the integral over the system volume is the total free energy F of the nonuniform system driving the kinetics. The integrand consists of three terms: a "constrained" local free energy density $f(c)$ of the system with effective "short range" interactions, having a double well shape below the critical temperature with minima at the compositions of the two equilibrium phases, a gradient square term giving the contributions to the interfacial energy and a long range elastic term, which can be rewritten as $|\tilde{Y}(\mathbf{k})\ \tilde{c}(\mathbf{k})|^2\, d\mathbf{k}$, with $\tilde{Y}$ given in (14). Equation (19), with a constant mobility σ, is essentially the one used by all continuum models of spinodal decomposition with elastic effects. (Some continuum models also consider an additional ordering field [20, 27].) Setting the denominator in (14) equal to 1 one can replace (19) by a differential equation [14]. In its simplest form the equation can be written as

$$\frac{\partial \phi(\mathbf{r}, t)}{\partial t} = -\nabla^2 \{ \phi(\mathbf{r}, t) - \phi^3(\mathbf{r}, t)$$

$$+ \nabla^2 \phi(\mathbf{r}, t) + w(\mathbf{r}, t) \}, \qquad (20)$$

where $\phi(\mathbf{r}, t) = c(\mathbf{r}, t) - \bar{c}$ and the elastic effects are all in the auxiliary function $w(\mathbf{r}, t) = \nabla^{-2}\phi(\mathbf{r}, t)$.

The general features of the cluster morphologies obtained by numerically integrating the continuum evolution equations are very similar to the results obtained from our microscopic model, *cf.* [13]–[22]. This opens the door to more detailed comparisons between the microscopic and macroscopic descriptions for systems with elastic interaction—something analogous to what has been done for rigid lattice models in recent years [24].

2.3. *Morphologies*

Given the three parameters $\{\Delta, \chi_{11}, \chi_{12}\}$, in the long range potential [14], the preferred directions of growth for the A and B rich clusters are obtained by finding the set of angles $\{\theta_0\}$ that globally minimizes $\tilde{Y}(\tilde{\mathbf{k}})$. In the absence of an external stress ($\chi_{11} = \chi_{12} = 0$), the minima are found at $\theta_0 = \{0, \pi/2\}$ when $\Delta < 0$, and $\theta_0 = \{\pm\pi/4\}$ when $\Delta > 0$, see [16]. In the case where uniaxial load is applied on the system ($\chi_{11} \neq 0$, $\chi_{12} = 0$) the local minima are still at $\theta_0 = 0$ and $\pi/2$ when $\Delta < 0$, but since

$$Y(0) = -Y_0(1 - \chi_{11}) \quad \text{and} \quad Y(\pi/2) = -Y_0, \tag{21}$$

the global minimum is at $\theta_0 = \pi/2$ if $\chi_{11} > 0$ (e.g. tensile stress along x-direction, when $\alpha > 0$) and $\theta_0 = 0$ if $\chi_{11} < 0$.

It is important to note that θ_0 is defined in Fourier space and thus the preferred growth direction in real space is perpendicular to the θ_0 plane. In particular the case $\chi_{11} > 0$ leads to clusters taking the form of stripes along the direction of the external load (the x axis with the definition of χ_{ij} above) while $\chi_{11} < 0$ (uniaxial compression if $\alpha > 0$ and tension if $\alpha < 0$) leads to stripes perpendicular to the external load. When the elastic anisotropy is positive ($\Delta > 0$), the presence of an external load shifts the minima away from the diagonals $\pm\pi/4$ towards new minima given by

$$\cos 2\theta_0 = -\frac{\xi\Delta + 4}{2\Delta(2 - \xi)} \tag{22}$$

to first order in χ_{11}. Thus the clusters take the form of stripes along directions given by angles $\pi/2 - \theta_0$ which are smaller (resp. larger) than $\pm\pi/4$ if $\chi_{11} > 0$ (resp. < 0) and approach the x (resp. y) axis as the load is increased.

In the case of pure external shear ($\chi_{11} = 0$, $\chi_{12} \neq 0$) and negative elastic anisotropy ($\Delta < 0$) the global minima of $Y(\theta)$ are shifted away from $\theta_0 = 0$ and $\pi/2$ and are given by

$$\sin 2\theta_0 = \frac{\chi_{12}}{\Delta(2 - \xi)} \tag{23}$$

to first order in χ_{12}. Hence, if $\chi_{12} > 0$ (resp. < 0), the clusters take the form of stripes along directions given by θ_0 and $\pi/2 - \theta_0$ with θ_0 increasing from 0 to $\pi/4$ as the external shear increases. Similarly, if $\chi_{12} < 0$ the stripes become closer to the $-\pi/4$ direction as $|\chi_{12}|$ increases. If the elastic anisotropy is positive $\Delta > 0$ the global minimum is given by $\theta_0 = \text{sign}(-\chi_{12})\pi/4$ and the clusters take the form of stripes along the direction of the external shear, i.e. $\pi/4$ if $\chi_{12} > 0$ and $-\pi/4$ if $\chi_{12} < 0$.

The various cases for uniaxial stress are summarized in Table 1. The results are in agreement with the energy analysis by Chang and Allen [3], as well as with the results by Nishimori and Onuki [14], for both uniaxial stress and shear.

3. COMPUTER SIMULATIONS

For the numerical simulations, we chose (as in I)

$$\lambda B = 2.18, \quad L_+/B = 0.48,$$
$$L_\times/B = 0.68, T_+/B = -0.16,$$

where B is the bulk modulus of the material introduced here in order to make the above parameters dimensionless. Since we are interested in the case of external stress in the x-direction, we put $\sigma^0_{ij} = \Lambda^0_{ijkl}\,\epsilon^0_{kl}$ explicitly:

$$\sigma^0_{11} = C^0_{11}\epsilon^0_{11} + C^0_{12}\epsilon^0_{22};$$
$$\sigma^0_{22} = 0 = C^0_{12}\epsilon^0_{11} + C^0_{11}\epsilon^0_{22};$$
$$\sigma^0_{12} = 0 = C^0_{44}\epsilon^0_{12}. \tag{24}$$

This leads to

$$\epsilon^0_{12} = 0 \quad \text{and} \quad \epsilon^0_{22} = -\frac{C^0_{12}}{C^0_{11}} \quad \epsilon^0_{11} = -\frac{L_\times - T_+}{L_\times + L_+}$$
$$\epsilon^0_{22} \approx -0.724\epsilon^0_{11}. \tag{25}$$

The constants appearing in the long-wave limit of the

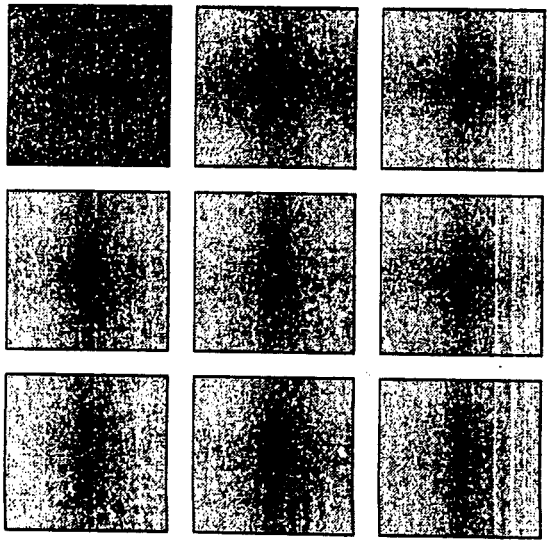

Fig. 4. Structure functions corresponding to the configurations shown in Fig. 3, left. Dark means large values of $S(\mathbf{k})$. The origin of $\mathbf{k}$ is in the center of the pictures.

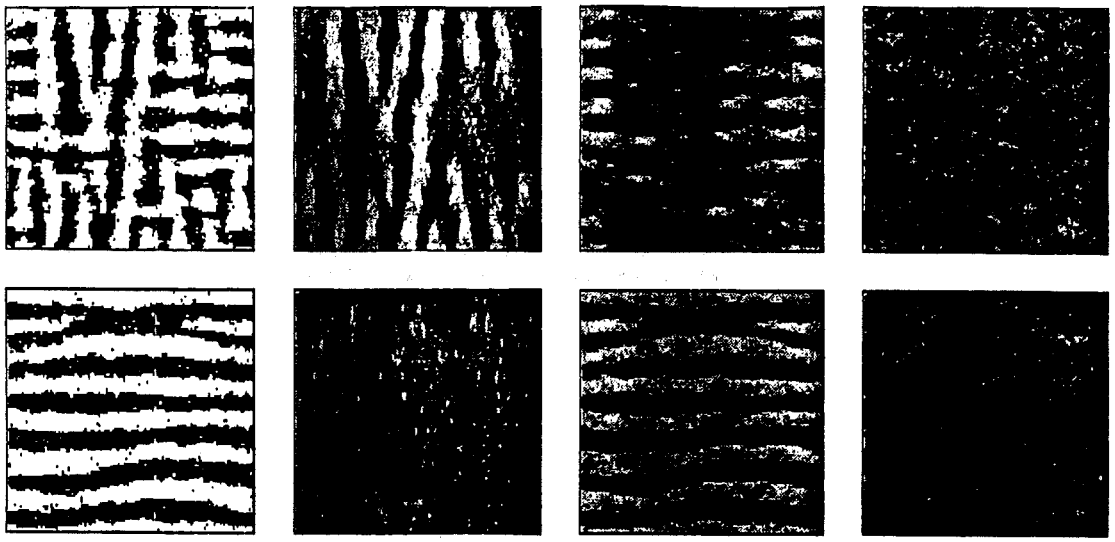

Fig. 5. Strains for the two different configurations shown in the first column (also shown in Fig. 3). ϵ_{11}, ϵ_{22} and ϵ_{12} are plotted in columns two to four, respectively. Dark means negative and white means positive values.

potential (14) then have the values

$$Y_0 \approx 3.91(1 - 0.276\zeta), \quad \Delta \approx -1.385,$$

$$\xi \approx 1.724, \quad \chi_{11} \approx 0.574\zeta, \quad \chi_{12} = 0, \qquad (26)$$

where we defined $\zeta = \alpha\epsilon_{11}^2$. Figure 2 shows plots of the potential $\Psi(\mathbf{k})$ for three values of ζ. The potentials at $\zeta = -0.1$ and $\zeta = 0.1$ are very similar, up to a 90° rotation, and we do not expect that they lead to any significant differences in the kinetics of coarsening, beside the actual direction of the clusters. Hence, in the computer simulations we only studied the cases $\zeta = 0$ and $\zeta = 0.1$.

Computer simulations were performed mainly on a 128×128 lattice (a 256×256 lattice was also used) at a temperature of $T = 0.8\,T_0 = 1.8J/k_B$ with ($\zeta = 0.1$) and without ($\zeta = 0$) external stress. Two "alloys" with concentration of (large) A-atoms $c = 0.5$ and $c = 0.2$ were considered. The simulations were performed using the algorithm described in I and II. In essence, it amounts to the Metropolis algorithm, where a nearest neighbor pair is chosen at random. If the exchange of the pair leads to a decrease in total energy, then the exchange is performed, if it leads to an increase δE, it is only done with probability $\exp(-\delta E/kT)$. Since the interaction potential is long-range, a special updating procedure (described in I) was used. From the configurations, the structure function as well as the strain fields were deduced. These strain fields

$$\epsilon_{11}(\mathbf{p}) = u_{1,1}, \quad \epsilon_{22}(\mathbf{p}) = u_{2,2}, \quad \epsilon_{12}(\mathbf{p}) = u_{1,2} + u_{2,1} \qquad (27)$$

were calculated for each "plaquette" of the square lattice in the way given in the first Appendix of I.

4. RESULTS

4.1. *Configurations*

Figure 3(a) shows a typical sequence of snap-shot pictures at $c = 0.5$, where rafting (with $\zeta = 0.1$) was

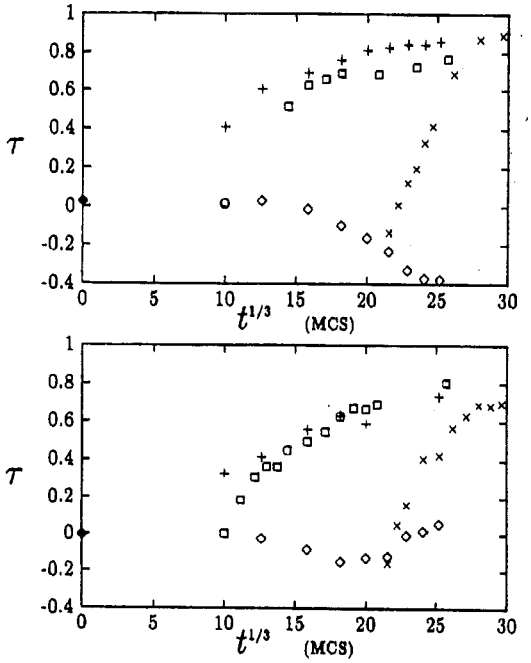

Fig. 6. Time evolution of the structure function asymmetry τ for alloys with composition $c = 0.5$ (top) and $c = 0.2$ (bottom). Runs without external stress ($\zeta = 0$) and starting from random initial configurations are indicated by ($\diamond$), ($+$), ($\square$) and ($\times$) show evolutions with external stress ($\zeta = 0.1$) starting from configurations prepared with no external stress for 0, 10^3 and 10^4 MCS, respectively. We used 10 independent computer runs on a 128×128 system.

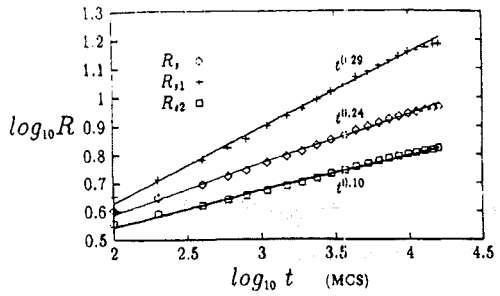

Fig. 7. R_{S1}, R_{S2} and R_S plotted vs time on double logarithmic scales for 10 independent runs on a 128 × 128 system with external stress ($\zeta = 0.1$) started a random distribution of atoms with composition $c = 0.5$.

started from three different initial configurations. The left column in Fig. 3 corresponds to a run started from randomly distributed A and B atoms, which corresponds to an alloy quenched from high temperature shown in the top left corner. Wavy stripes are seen to develop and to thicken with time. The center column in Fig. 3(a) shows a run started from a situation obtained after 1000 Monte-Carlo Steps (MCS) (starting with the same top left corner configuration) at the same temperature, but without external stress. The right column, finally, shows a similar run started from a configuration obtained after 10^4 MCS without external stress. One can clearly see how the vertical stripes gradually disappear, leading finally to a configuration where only horizontal stripes persist. Even though the time elapsed is the same in all three columns, there is a considerable difference in the way the stripes thicken. While they stay almost of the same thickness in the right column, there is a considerable coarsening of the structure in the left column.

A picture similar to Fig. 3(a), but for an alloy composition of $c = 0.2$ is shown in Fig. 3(b). Again, the first line shows configurations obtained without external stress after letting the system evolve for 0, 10^3 and 10^4 MCS. As already discussed in II, plate-like precipitates oriented along lines and columns of the lattice develop under these conditions. When the external stress is applied, the configurations evolve as shown in the second and, finally, the third line of graphs in Fig. 3(b). Again, the last configurations are rather similar regardless of the starting configurations and contain only precipitates oriented along the horizontal direction. While in the first column (where rafting started from a homogeneous mixture of A and B atoms) some coarsening of the plates is visible, the evolution in the right column is mainly characterized by the gradual disappearance of all vertically oriented precipitates.

4.2. *Structure function*

In the course of the simulations we calculated the structure function $S(\mathbf{k}) = |\Sigma_{\mathbf{p}} \gamma(\mathbf{p}) e^{i\mathbf{k}\cdot\mathbf{p}}|^2$, by using the (squared) fast Fourier transforms of the configurations. As an example, we show in Fig. 4 grey-scale representations of the structure functions corresponding to the configurations shown in Fig. 3(a).

When no external stress is applied, the structure function shows, in agreement with the results in I and II, a flower-like pattern. This pattern is increasingly anisotropic when the structure coarsens, but it keeps roughly the quadratic symmetry of the lattice. The pattern, predicted by mean-field analysis (see I), reproduces quite well the **k**-space potential for $\zeta = 0$ with the structure function highest were the potential is lowest, see Fig. 2. Following a quench the pattern takes longer to develop at small **k**, because long-wavelength fluctuations take much longer to relax than those with short wavelengths.

When a uniaxial external stress is applied to the system, the quadratic symmetry is broken and, as seen in Fig. 2(a) and (b) stripe-like domains appear. This is manifested in the structure function by the fact that it concentrates more and more into a vertical streak. Again, this in excellent agreement with the corresponding shape of the interaction potential in Fig. 1.

4.3. *Elastic strains*

In order to get an idea for the influence of the elastic part of the energy (as opposed to the

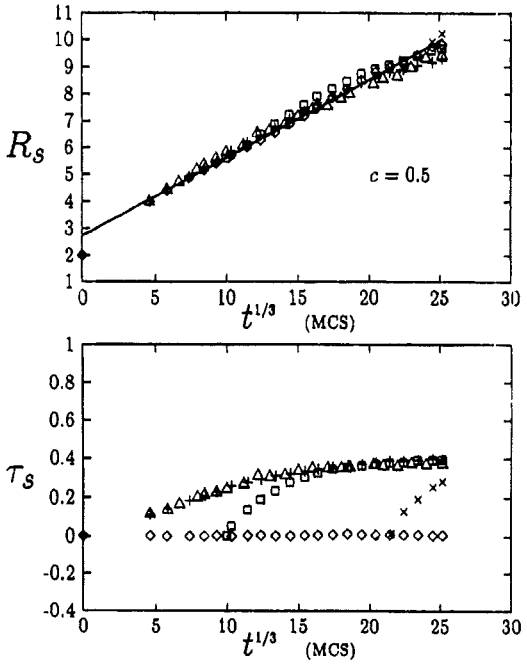

Fig. 8. R_S and τ_S for $c = 0.5$ as a function of time for random initial configurations and no external stress on the system (◇), and for external stress on the system started with random initial configurations (+) or with initial configurations prepared for 1000 MCS (□) or 10,000 MCS (×) without external stress. The system size was 128 × 128 and all data have been averaged over 10 independent runs. Also shown are results obtained from one individual run on a 256 × 256 system (△) started from a random initial configuration with external stress.

"chemical" short-range part), we have determined in a few cases also the elastic strains associated with a given configuration. These strains are related linearly to the configuration variables, the exact relations being obtained in the course of the minimization process that led from (8) to (11).

Figure 5 shows—for two examples—the configuration (top line), the values of $\epsilon_{11} - \epsilon_{11}^0$, $\epsilon_{22} - \epsilon_{22}^0$, and ϵ_{12} (second to fourth line in Fig. 5) on a pseudo-grey scale. ϵ_{11} is the total strain along the horizontal direction, while ϵ_{11}^0 is the (homogeneous) part of the strain directly due to the stress applied from outside. These quantities are the ones that actually enter the elastic energy of the system (8). The grey-scale is defined in such a way that average grey means zero, while lighter shades mean positive and darker ones negative values. It can be seen in the second column and second line of Fig. 5 that—besides a number of localized light and dark spots—the picture is just average grey, meaning only very small strains, $\epsilon_{11} - \epsilon_{11}^0$, in the horizontal direction. The picture below it, on the contrary, shows a succession of light and dark stripes reproducing almost exactly the stripes in the configuration (top of second column in Fig. 5). This means that the vertical strain, $\epsilon_{22} - \epsilon_{22}^0$, is positive inside the regions containing mostly large A-atoms (appearing white in the plot of the configuration) and negative inside the regions containing mostly the small B-atoms. The reason why this effect is seen for $\epsilon_{22} - \epsilon_{22}^0$ but not for $\epsilon_{11} - \epsilon_{11}^0$, is due to the fact that in the direction along the stripes, the lattice spacing is constrained by the periodic boundary conditions of the lattice and cannot deviate much from its average value, while in the vertical direction a small lattice spacing in the black stripes can be compensated by a large spacing in the white stripes.

In the case of a configuration obtained without external stress (meaning that $\epsilon_{11}^0 = \epsilon_{22}^0 = 0$) shown in the left column of Fig. 5, the same type of effect can be seen: The strains are very small along the direction of the stripes, while they are large perpendicularly to the stripes. This appears, e.g. in the second picture (from the top of the left column) where only vertical stripes are visible as clear and dark regions. In regions of the configuration where horizontal stripes prevail, ϵ_{11} is close to zero (that is average grey in the figure). Similarly, where vertical stripes dominate, ϵ_{22} is close to zero (third picture from top).

In all cases, the diagonal shear ϵ_{12} (bottom line in Fig. 5) shows large (positive or negative) values at edges and tips of domains. A typical example can be seen in the upper left corner of the configuration in the right column, where a black stripe comes in from the left and ends abruptly. Large positive as well as negative shears appear in this region.

4.4. *Kinetics of symmetry breaking*

As already mentioned, the introduction of an external uniaxial stress breaks the four fold lattice symmetry of the potential and, hence, of the domain morphology. This leads ultimately to the formation of stripes either perpendicular or parallel to the external strain. In order to get a quantitative measure for the amount of symmetry breaking, we have defined a parameter τ as the asymmetry of the structure function in the following way:

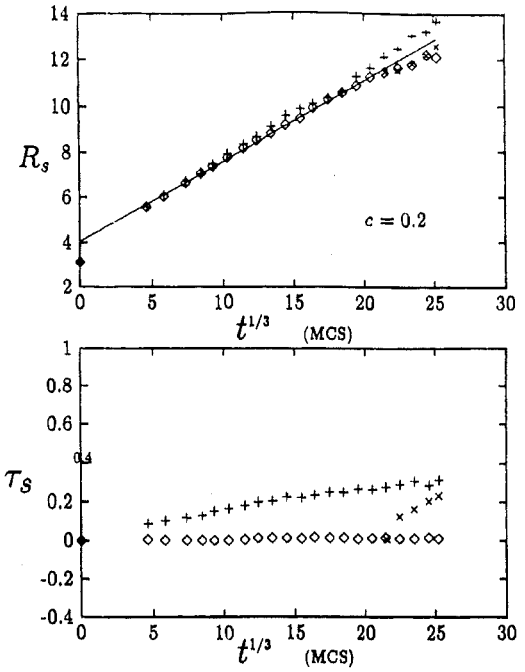

Fig. 9. R_S and τ_S for $c = 0.2$ with the same symbol convention as in Fig. 8.

Let us call $I(h, l) = |S(\mathbf{k})|^2$, where $\mathbf{k} = 2\pi(h\mathbf{e}_1 + l\mathbf{e}_2)$ and h, l are integers in the range $-L/2, \ldots, L/2 - 1$, for a lattice with $L \times L$ sites. Then we define

$$\tau \equiv (J_+ - J_-)/(J_+ + J_-), \tag{28}$$

where

$$J_+ = \sum_{|h| < |l| < L/2} I(h, l) \quad \text{and} \quad J_+ = \sum_{|h| < |l| < L/2}$$

$$I(h, l) \quad \text{and} \quad J_- = \sum_{|l| < |h| < L/2} I(h, l).$$

With this definition, τ is zero for a symmetric structure function. If the domain morphology consisted of perfect horizontal stripes, then all the structure function would be concentrated at $h = 0$, yielding $\tau = 1$ for the asymmetry parameter. If, on the contrary, there was a tendency to form vertical stripes, τ would be negative and for perfect vertical stripes would equal to -1.

Figure 6(a) shows τ determined for an alloy with composition $c = 0.5$ treated at the temperature $kT/J = 1.8$ under various conditions. A first run without external stress is plotted by diamonds. In this

run, τ stayed first close to 0 and then started to deviate towards negative values. The configuration corresponding to the time 10^4 MCS is shown in Fig. 3(a) top right. The negative value for τ corresponds to the fact that there were more vertical than horizontal stripes in the configuration, as a result of fluctuations. Nonetheless, when the external stress was turned on, the parameter τ started to increase quickly and after an additional 1000 MCS it became again positive (crosses in Fig. 6(a)). After a long time, τ reached a value of 0.8–0.9, and did not increase further. The same was found for cases where the external stress field was turned on immediately after quench (plus-signs in Fig. 6(a)) or after 10^3 MCS without external stress (squares in Fig. 6(a)). In all cases a limiting value of 0.8–0.9 was reached rapidly and then τ remained at approximately this value. Since $\tau = 1$ would correspond to the residual waviness of the stripes that seems to subsist in all cases even after very long times under uniaxial stress (see bottom line in Fig. 3(a)).

Figure 6(b) shows a similar graph, but for the alloy with a composition of $c = 0.2$. Again the asymmetry fluctuates around zero for an alloy without external stress (diamonds). With uniaxial external stress applied, starting either from a random mixture of A and B (pluses) or after pretreatment without external stress for 10^3 (squares) or 10^4 MCS (crosses), the asymmetry goes up very rapidly to a value of about 0.8.

4.5. Time evolution of the interfaces

A measure for the total amount of interface pointing into horizontal and vertical direction was determined via the quantities

$$S_i = \frac{1}{2}\sum_{\mathbf{p}}\Big(1 - \gamma(\mathbf{p})\gamma(\mathbf{p} + a\mathbf{e}_i)\Big), \tag{29}$$

periodic boundary conditions for the $L \times L$ lattice being understood. S_i is just the number of nearest neighbor broken bonds in the horizontal direction

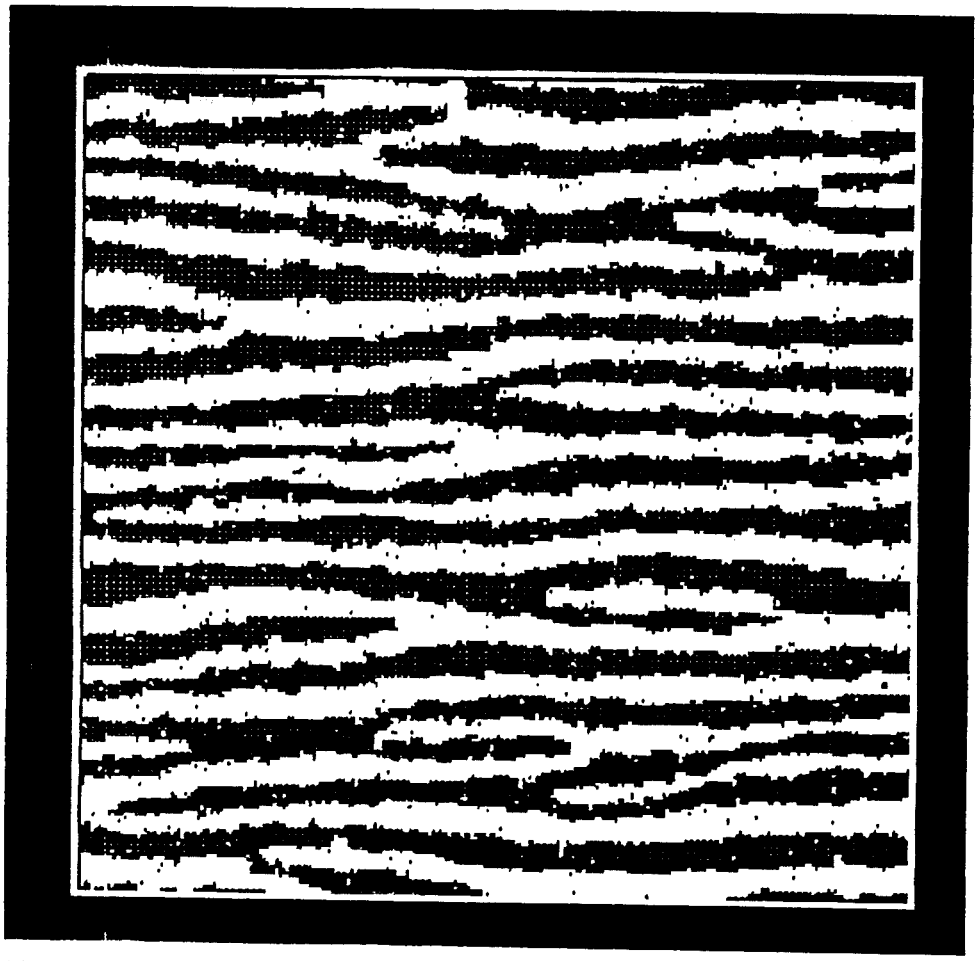

Fig. 10. Snapshot of a configuration obtained by starting from a random initial configuration with an equal amount of A and B atoms on a 256 × 256 lattice and letting the system evolve with an applied external stress ($\zeta = 0.1$) at a temperature $T = 0.8T_0 = 1.8J/k_B$ for time $t = 32{,}000$ MCS.

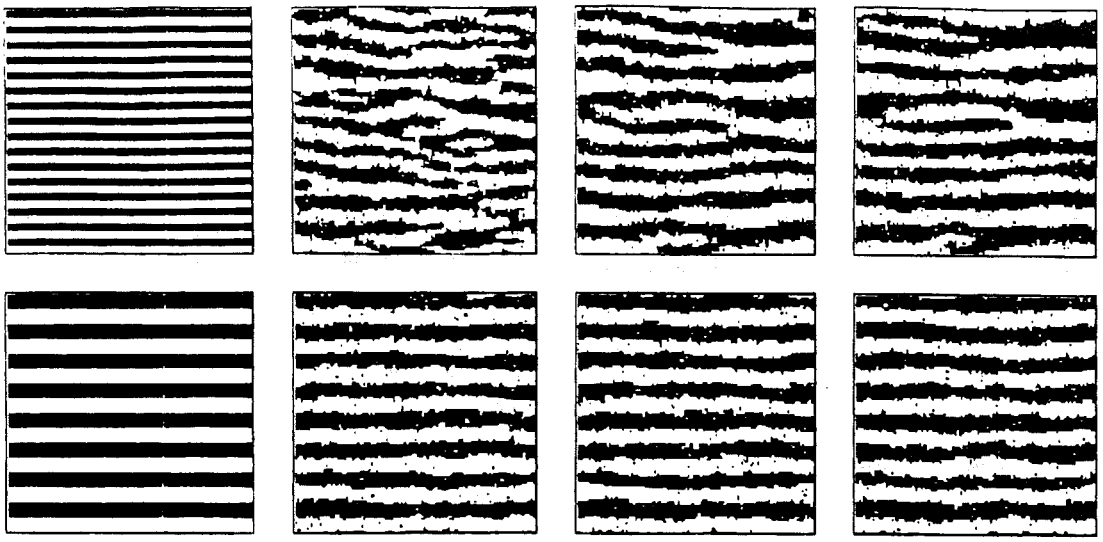

Fig. 11. Snapshots of the configurations after 0, 10, 20 and 30 kMCS (from left to right) under external stress ($\zeta = 0.1$) starting from perfect stripes, on a 128×128 lattice.

and, therefore, a measure for the length of the interfaces projected onto the vertical direction. S_2 has a similar meaning (all directions being rotated 90°) and $S_1 + S_2$ is a measure for the total amount of interface present in the system.

In an isotropic coarsening process [28, 29], with the volume fraction of the phases constant, the interface S is expected to change in time as $1/R$, where R is an average domain size. In analogy, we define length scales R_S, R_{S_1}, and R_{S_2} by

$$R_S = 2L^2/(S_1 + S_2),$$

$$R_{S_i} = L^2/S_i, \quad \text{(where } i = 1, 2) \tag{30}$$

For perfectly rectangular domains with interfaces pointing along lines and columns of the lattice, R_{S_1} would be a measure for the length of the domains in the horizontal and R_{S_2} for the width of the domains in the vertical direction. R_S, defined as the inverse of the total interface, is then just an average of R_{S_1} and R_{S_2}. Figure 7 shows these three length scales as a function of time for the case $c = 0.5$, started from a homogeneous distribution of A and B atoms, the alloy being subjected to external strain (with $\zeta = 0.1$). It is apparent in the figure that R_{S_1} grows much faster than R_{S_2}, the time-dependence of their average R_S being intermediate. On a double-logarithmic scale (see Fig. 7), the behavior of these lengths scales as a function of time may be represented roughly by a straight line, corresponding to a power-law behavior t^m of the length scales. The fitted values are $m \approx 0.10$ for R_{S_2}, $m \approx 0.29$ for R_{S_1}, and $m \approx 0.24$ for R_S.

These log–log plots are however far from conclusive. As an alternate representation we checked whether R_S could be represented as a linear function of t^α, $\alpha = \frac{1}{3}$ being the usual time dependence of the average domain size in the Ising model with [16] or without [29] elastic interactions. A plot of R_S vs $t^{1/3}$,

$$R_S \approx Kt^{1/3} + K_0 \tag{31}$$

is shown in Fig. 8 and the fit seems quite good. Moreover, the constants K and K_0, were found to be independent of the initial configuration and of whether external stress was applied or not. We note further that equation (31) describes the time evolution over the whole time period where data were obtained, while the power-law description (see Fig. 7) only works in a narrower time-range. By comparing Fig. 8 with a plot of R_S vs $t^{1/4}$, which does not give quite as good a fit, we are inclined to believe that the exponent $m \approx \frac{1}{4}$ is only an effective exponent which would continue to increase (according to equation (31)) towards 1/3 when time increases. This would be in accord with the idea of Huse [30] who first used an expression of type (31) to account for contributions of interface diffusion to the coarsening. Huse assumed that for large t, R_S satisfies the equation

$$\frac{dR_S}{dt} \approx \frac{K}{3R_S^2}(1 + 2K_0/R_S). \tag{32}$$

For $K_0 = 0$, (32) corresponds to the equation derived by Lifshitz, Slyozov and Wagner [28] to describe coarsening by volume diffusion. The additional term describes coarsening by interface diffusion [30]. If, on the other hand, K_0 is large compared to R_S, then $R_S \sim t^{1/4}$, while if K_0 is much smaller than $R_S \sim t^{1/3}$. Hence, if interface diffusion is important one would expect a growth exponent $m = 1/4$ at intermediate times which should cross-over to $m = 1/3$ at very late times. This may explain the differences between the exponents found in Figs 7 and 8. It should also be remembered that finite size effects are likely to play a role here at late times.

The time evolution of R_S may also be compared to the one of the first zero R_C of the radially averaged

correlation function, which is often used to characterize the domain size. R_C was determined and fitted to equation (31) in II for the same temperature and compositions as in Figs 8 and 9, but only in the case without external stress. Besides a multiplicative factor β ($\beta = 0.92$ in the case $c = 0.5$ and $\beta = 0.66$ in the case of $c = 0.2$), the time behavior of R_C and R_S are equal. The time-dependence of βR_C is indicated by a full line in Figs 8 and 9.

4.6. Waviness of the stripe-like domains

It turns out that the values obtained for R_S are almost exactly the same for a run starting with a homogeneous distribution of A and B atoms, but without any externally applied stress. The only difference is that instead of the symmetry breaking visible in Fig. 7, $R_{S_\perp} \approx R_{S_\parallel} \approx R_S$ in the case without external stress. In order to characterize the symmetry breaking in the distribution of the interfaces, we

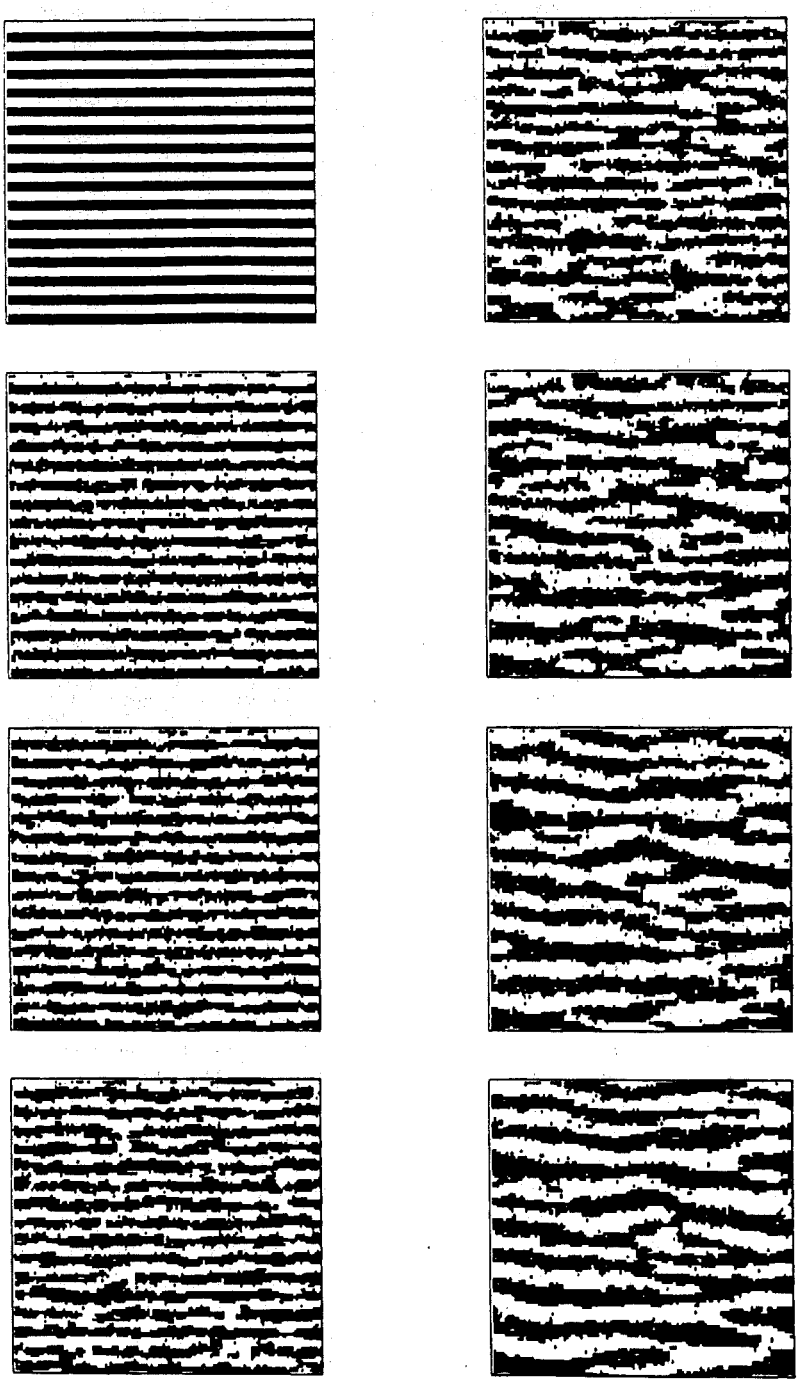

Fig. 12. Snapshots of the configurations after 0, 1, 2, 4 kMCS (first column) and 6, 8, 10 and 12 kMCS (second column) under external stress ($\zeta = 0.1$) starting from perfect stripes, on a 128 × 128 lattice.

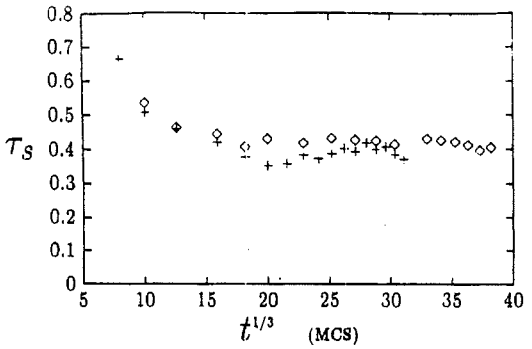

Fig. 13. Evolution of the surface asymmetry τ_S as a function of time for initial configurations consisting of 8 (◇) and 16 (+) stripes (snapshots shown in Fig. 11).

define a surface asymmetry τ_S as

$$\tau_S = \frac{S_1 - S_2}{S_1 + S_2}. \tag{33}$$

R_S and the asymmetry τ, are plotted for a number of cases in Fig. 8 ($c = 0.5$) and Fig. 9 ($c = 0.2$). These include runs starting from a homogeneous distribution with (triangles) and without (diamonds) external stress, as well as runs with external stress started after 10^3 (full squares) and after 10^4 MCS (discs) pretreatment at the same temperature but without external stress.

The surface asymmetry τ_S stays close to 0 for the alloy without external stress (diamonds in Fig. 8) and increases to about 0.4 when external stress is applied. For both $c = 0.5$ and $c = 0.1$, $\tau_S \approx 0.4$ seems to be a limiting value, even though in the case of perfect stripes τ_S should be equal to 1. The reason why τ_S stays so much smaller cannot be due to the monomers present inside the segregated phases at finite temperature, which contribute to both S_1 and S_2, since their number is fairly small. The main effect responsible for the saturation of τ_S at a value of about 0.4, appears to be the strong waviness of the interfaces that can be seen in Fig. 3. Indeed, even after very long times, a typical configuration of atoms still shows wavy stripes, as seen in Fig. 10 for a 256×256 lattice started from an initially random distribution. In this run the value of τ_S also saturated at about 0.4 (see Fig. 8), which shows the independence of this value from the lattice size.

In order to see whether this waviness remains true when started from an initial configuration with perfect stripes, we have performed several runs starting with perfectly straight stripes. Examples are shown in Figs 11 and 12, where series of configurations are drawn. It is clear that the configuration with perfect stripes is not stable and that the stripes become wavy and broken very rapidly. A reduction in the number of stripes then occurs when two such wavy stripes or segments of stripes meet and ultimately join. This process is, in fact, the major reason for the coarsening of stripe-like patterns as in Fig. 3(a), left column.

The time-evolution of the surface asymmetry τ_S, which started out to be equal to 1 for the perfect stripes at time = 0, is shown in Fig. 12. We see that τ_S decreases rapidly at first and that after a few thousand Monte-Carlo steps it oscillates around a value close to 0.4, irrespective of the initial number of stripes present in the configurations. We plan to investigate further the dependence of τ_S on the external strain and on the temperature.

5. DISCUSSION

It is very gratifying that despite the many obvious simplifications the predictions of the model are in good agreement with experimental results. They thus provide a microscopic model for comparison with experiments and continuum models.

- Stripe-like structures develop with orientation depending on the difference in lattice constants and elastic moduli of the two phases as well as the direction of applied stress, in good agreement with previous work [1–10].
- The four-fold symmetry in the structure function in the cubic material is broken gradually when external stress is applied. The same patterns were observed by small-angle X-ray scattering during precipitate rafting in Ni-base superalloys [10].
- The resulting asymmetry of the alloy monitored by the asymmetry of the structure factor τ and of the interfaces in x and y direction τ_S is increasing but saturating at typical values of about $\tau \approx 0.8$ and $\tau_S \approx 0.4$. A similar effect was observed during rafting in Ni-base alloys where the aspect ratio of the precipitates ρ was found from small-angle scattering and transmission microscopy [10] to saturate at about $\rho \approx 4$, corresponding to an asymmetry $\tau = (\rho - 1)(\rho + 1) \approx 0.6$.
- A strong inherent "waviness" of the interfaces between phases was identified as a possible reason for this saturation (Figs 11 and 13). Strong waviness was also found in experiments on Ni-based alloys [10].
- The average domain size R_S was found to increase with time t in a manner consistent with, $R_S \sim Kt^{1/3} + K_0$. This is similar to phase segregation models with or without elastic interactions. It suggests that the short-range chemical interaction is mainly responsible for this aspect.

The striking similarities between the results in the present model and experimental observation by small-angle scattering [10] and electron microscopy [1–10] seems to support the idea that elastic interaction could, indeed, be at the origin of the rafting process. This stands in contrast to the accumulation of dislocations always found associated with directional coarsening [8, 10], which clearly indicates that dislocations participate in the rafting process. A possible source for such dislocations,

suggested by the present results, could be the extreme waviness of perfectly coherent interfaces subjected to considerable stresses. This waviness of the interfaces raises a number of issues concerning the stability of interfaces in the presence of elastic interactions that would be well worth exploring further. Also, since two-dimensional simulations cannot differentiate between clusters taking the shape of elongated needles aligned along the stress axis and broad plates viewed edge on, it would be very instructive to compare three-dimensional simulations with experiments.

Acknowledgements—We are grateful to R. Cahn, M. Fährmann, A. Khachaturyan, O. Paris and O. Penrose for discussions. Work was supported by NSF Grant 92-13424 4-20946 and DMR-9419393. P.F. also acknowledges support by the Fonds zur Förderung der Wissenschaftlichen Forschung (Project S5601).

REFERENCES

1. Tien, J. K. and Copley, S. M., *Metall. Trans.*, 1971, **2**, 215.
2. For a recent short review see, e.g. Socrate, S. and Parks, D. M., *Acta metall. mater.*, 1993, **41**, 2185.
3. Linear elastic models for rafting are reviewed in: Chang, J. C. and Allen, S. M., *J. Mater. Res.*, 1991, **6**, 1843.
4. Miyazaki, T., Nakamura, K. and Mori, H., *J. Mater. Sci.*, 1979, **14**, 1827.
5. Nathal, M. V., MacKay, R. A. and Miner, R. V., *Metall. Trans.*, 1989, **20A**, 133.
6. Feller-Kniepmeier, M. and Link, T., *Metall. Trans.*, 1989, **20A**, 1233.
7. Carry, C. and Strudel, J. L., *Acta metall.*, 1977, **25**, 767; 1978, **26**, 859.
8. Pollock, T. M. and Argon, A. S., *Acta metall. mater.*, 1994, **42**, 1859.
9. Buffiere, J. Y. and Ignat, M., *Acta metall. mater.*, 1995, **43**, 1791.
10. Paris, O., Fährmann, E., Pollock, T. M. and Fratzl, P., *Acta mater.*, 1997, **45**, 1085.
11. Pineau, A., *Acta metall.*, 1976, **24**, 559.
12. Johnson, W. C., Birkenpas, M. B. and Laughlin, D. E., *Acta metall.*, 1988, **36**, 3149.
13. Khachaturyan, A. G., *Theory of Structural Transformations in Solids*, Wiley, New York, 1983.
14. Nishimori, H. and Onuki, A., *Phys. Rev. B*, 1990, **42**, 980.
15. Gayda, J. and Srolovitz, D. J., *Acta metall.*, 1989, **37**, 641.
16. Fratzl, P. and Penrose, O., *Acta metall. mater.*, 1995, **43**, 2921.
17. Fratzl, P. and Penrose, O., *Acta mater.*, 1996, **44**, 3227.
18. Lee, J. K., *Scripta Met. Mat.*, 1995, **32**, 559; Lee, J. K., *Metall. Mater. Trans. A*, 1996, **27**, 1449.
19. Laberge, C. A., Fratzl, P. and Lebowitz, J. L., *Phys. Rev. Lett.*, 1995, **75**, 4448.
20. Wang, Y., Chen, L.-Q. and Khachaturyan, A. G., *Acta metall. mater.*, 1993, **41**, 279.
21. Cook, H. E. and DeFontaine, D., *Acta metall.*, 1969, **17**, 915.
22. Khachaturyan, A. G., *Soviet Phys. Crystallogr.*, 1965, **10**, 256.
23. Hohenberg, P. C. and Halperin, B. I., *Rev. Mod. Phys.*, 1977, **49**, 435.
24. Langer, J. S. in *Solids Far from Equilibrium*, ed. C. Godreche. Cambridge University Press, Cambridge, England, 1992.
25. Cahn, J., *Acta metall.*, 1962, **10**, 179.
26. Onuki, A. and Nishimori, H., *Phys. Rev. B*, 1991, **43**, 13649.
27. Sagui, C., Somoza, A. M. and Desai, R., *Phys. Rev. E*, 1994, **50**, 4865.
28. Lifshitz, I. M. and Slyozov, V. V., *J. Phys. Chem. Solids*, 1961, **19**, 35; Wagner, C., *Z. Elektrochem.*, 1961, **65**, 581.
29. Fratzl, P., Lebowitz, J. L., Penrose, O. and Amar, J., *Phys. Rev. B*, 1991, **44**, 4794.
30. Huse, D. A., *Phys. Rev. B*, 1986, **34**, 7845.